JEM Journal of Experimental Medicine

BRIEF DEFINITIVE REPORT

SARM1 deficiency up-regulates XAF1, promotes neuronal apoptosis, and accelerates prion disease

Caihong Zhu*, Bei Li*, Karl Frontzek, Yingjun Liu, and Adriano Aguzzi

SARM1 (sterile α and HEAT/armadillo motif–containing protein) is a member of the MyD88 (myeloid differentiation primary response gene 88) family, which mediates innate immune responses. Because inactivation of SARM1 prevents various forms of axonal degeneration, we tested whether it might protect against prion-induced neurotoxicity. Instead, we found that SARM1 deficiency exacerbates the progression of prion pathogenesis. This deleterious effect was not due to SARM1-dependent modulation of prion-induced neuroinflammation, since microglial activation, astrogliosis, and brain cytokine profiles were not altered by SARM1 deficiency. Whole-transcriptome analyses indicated that SARM1 deficiency led to strong, selective overexpression of the pro-apoptotic gene XAF1 (X-linked inhibitor of apoptosis-associated factor 1). Consequently, the activity of pro-apoptotic caspases and neuronal death were enhanced in prion-infected *SARM1*$^{-/-}$ mice. These results point to an unexpected function of SARM1 as a regulator of prion-induced neurodegeneration and suggest that XAF1 might constitute a therapeutic target in prion disease.

Introduction

SARM1 (sterile α and HEAT/armadillo motif–containing protein), a member of MyD88 (myeloid differentiation primary response gene 88) family (MyD88-5), is a highly conserved cytosolic adaptor molecule that negatively regulates TRIF (Toll/interleukin-1 receptor [TIR] domain–containing adaptor inducing interferon-β)-mediated TLR signaling in mammalian cell cultures (Carty et al., 2006). SARM1 is expressed primarily by neurons in the mouse brain (Kim et al., 2007). By decreasing the association of JNK3 with mitochondria, SARM1 deficiency protects neurons from death due to oxygen and glucose deprivation (Kim et al., 2007). Similarly, *SARM1*$^{-/-}$ mice also show protection from neuronal injury induced by vesicular stomatitis virus and La Crosse virus (Hou et al., 2013; Mukherjee et al., 2013). On the other hand, SARM1 restricts neurotropic West Nile virus (WNV) infection by modulating microglia activation and cytokine production (Szretter et al., 2009). These studies suggest an involvement of SARM1-mediated innate immunity in neuronal death.

Two independent genetic screens identified SARM1 as a mediator of Wallerian axonal degeneration after acute nerve injury (Osterloh et al., 2012; Gerdts et al., 2013). SARM1 triggers Wallerian degeneration by activating the MAPK cascade, through nicotinamide adenine dinucleotide (NAD^+) depletion (Gerdts et al., 2015, 2016; Yang et al., 2015; Sasaki et al., 2016; Essuman et al., 2017; Walker et al., 2017) and by stimulating Ca^{2+} influx into injured axons (Loreto et al., 2015). In addition, SARM1 mediates axon degeneration in traumatic brain injury and vincristine-induced peripheral neuropathy (Geisler et al., 2016; Henninger et al., 2016). These findings raise the question of whether SARM1 might participate to further neurodegenerative pathologies.

Prion diseases are a group of neurodegenerative disorders characterized by the deposition of PrP^{Sc}, a misfolded isoform of cellular prion protein (PrP^{C}), in the central nervous system and other organs (Aguzzi and Zhu, 2012). Progressive accumulation of PrP^{Sc} in the central nervous system leads to lethal encephalopathies associated with neuronal loss, spongiform change, and neuroinflammation (Aguzzi et al., 2013). The contribution of innate immunity to prion pathogenesis remains to be fully understood (Aguzzi and Zhu, 2017). Axonal degeneration is an early feature of most neurodegenerative disorders including prion diseases (Conforti et al., 2014). Axonal degeneration and synaptic loss are observed both in Creutzfeldt-Jakob disease and animal models of prion diseases (Guiroy et al., 1989; Jeffrey et al., 1995; Liberski et al., 1995; Liberski and Budka, 1999; Ferrer, 2002; Gray et al., 2009; Reis et al., 2015) and often precede neuronal death. However, the mechanism of axon degeneration and its contribution to prion pathogenesis remain unknown.

In this study, we aimed to ascertain whether SARM1-mediated innate immunity and/or SARM1-dependent axon

Institute of Neuropathology, University of Zurich, Zurich, Switzerland.

*C. Zhu and B. Li contributed equally to this paper; Correspondence to Adriano Aguzzi: adriano.aguzzi@usz.ch.

degeneration might play a role in prion pathogenesis. We found that SARM1 expression was decreased upon prion infection. Prion inoculation experiments revealed that disease progression was moderately accelerated by SARM1 deficiency. Analysis of the neuroinflammatory response failed to find any difference between prion-infected *SARM1*$^{-/-}$, *SARM1*$^{+/-}$, and their WT littermates (*SARM1*$^{+/+}$), indicating that SARM1-mediated innate immunity does not account for the deceleration of prion progression. We then performed a genome-wide transcriptome analysis of SARM1$^{+/+}$ and SARM1$^{-/-}$ mouse brains with or without prion infection. Surprisingly, we found that SARM1 ablation led to an up-regulated expression of the pro-apoptotic gene X-linked inhibitor of apoptosis (XIAP)–associated factor 1 (XAF1; Liston et al., 2001), resulting in enhanced pro-apoptotic caspase activity and neuronal death in prion-infected *SARM1*$^{-/-}$ mice. In vitro experiments demonstrated that the increased susceptibility of SARM1-silenced neuronal cells to apoptotic stimuli were abrogated by ablating XAF1. Hence, SARM1 deficiency sensitizes mice to prion-induced neurodegeneration, probably by creating an XAF1-driven pro-apoptotic environment within neurons.

Results and discussion

Down-regulation of SARM1 expression in prion-infected mouse brains

To determine whether the expression of SARM1 is altered by prion infection, we performed quantitative real-time PCR (qRT-PCR) on mRNA isolated from terminally scrapie-sick WT C57BL/6 mice infected with the Rocky Mountain Laboratory strain of mouse-adapted scrapie prions (passage #6, therefore named RML6). For comparison, we used age-matched WT C57BL/6 mice inoculated with noninfectious brain homogenates (NBHs). We found that *Sarm1* mRNA was significantly reduced in prion-infected mouse brains (Fig. 1 A). In contrast, other members of TLRs and adaptor molecules were either up-regulated or unchanged upon prion infection (Fig. 1, B–D), suggesting that SARM1 is unique among TLR-associated molecules in its modulation by prion infection.

We then performed Western blot analyses to assess the SARM1 protein level in RML6- or NBH-inoculated mouse brains. Again, we observed that the SARM1 protein level was significantly suppressed in RML6-infected C57BL/6 mouse brains (Fig. 1, E and F; and Fig. S1). When the SARM1 signal was normalized against neuronal markers, the relative SARM1 level was still lower in RML6-infected samples compared with NBH-treated samples, indicating that the suppression of SARM1 in prion-infected mouse brains was not solely due to neuronal death at the terminal stage of disease (Fig. 1, F and G; and Fig. S1) but rather by prion-specific events (such as prion-induced stresses to the neurons).

SARM1 deficiency resulted in accelerated prion progression

We found that SARM1 deficiency does not affect the expression of PrP^C in mouse brains (Fig. 2, A and B). To determine whether the SARM1-mediated innate immune responses and/or axonal degeneration may influence prion pathogenesis, we intracerebrally inoculated *SARM1*$^{-/-}$, *SARM1*$^{+/-}$, and *SARM1*$^{+/+}$ littermates with RML6 prions. We found that SARM1 deficiency accelerated prion disease. *SARM1*$^{-/-}$ mice experienced significantly shortened incubation times compared with isogenic WT littermates (median survival, 166 d after inoculation [dpi] for *SARM1*$^{-/-}$ vs. 176 dpi for WT littermates; P = 0.01). *SARM1*$^{+/-}$ mice showed a trend toward acceleration that did not reach statistical significance (median survival, 171 dpi; Fig. 2 C). These results indicate that SARM1 deficiency accelerates prion progression and suggest a possible effect of SARM1 haploinsufficiency, implying that SARM1 instead plays a neuroprotective role in prion pathogenesis. The effect of SARM1 deficiency on prion progression was moderate, but it was statistically significant, and its magnitude is comparable to that seen in other genetically modified animal models or upon pharmacological treatments (Sakai et al., 2013; Grizenkova et al., 2014; Sorce et al., 2014; Herrmann et al., 2015; Zhu et al., 2016; Goniotaki et al., 2017).

To compare the prion pathogenesis between *SARM1*$^{-/-}$, *SARM1*$^{+/-}$, and *SARM1*$^{+/+}$ mice, brains were collected synchronously from prion-infected *SARM1*$^{-/-}$, *SARM1*$^{+/-}$, and *SARM1*$^{+/+}$ mice at 112 dpi, a time point at which mice did not reach terminal stage. Histology of brains from *SARM1*$^{-/-}$, *SARM1*$^{+/-}$, and *SARM1*$^{+/+}$ mice harvested at 112 dpi failed to reveal any obvious difference in lesion patterns and PrP^{Sc} deposition in different areas (Fig. 2 D). Western blots detecting proteinase K (PK)–resistant prion protein (PrP^{Sc}) confirmed a similar level of PrP^{Sc} accumulation at 112 dpi (Fig. 2 E). Therefore, SARM1 deficiency neither changed prion-induced lesion pattern nor altered PrP^{Sc} accumulation.

Prion diseases are associated with axon degeneration. Accordingly, we found neurofilaments NF70 and NF200 to be decreased in prion-infected mouse brains (Fig. 2, F–L; and Fig. S1). SARM1 is required for axon degeneration induced by various stimuli. However, in the RML mouse model of prion disease, prion pathogenesis was aggravated in *SARM1*$^{-/-}$ mice. The acceleration of prion progression by SARM1 deficiency therefore implies that SARM1-mediated axon degeneration does not play a major role in prion pathogenesis. Consistent with this assertion, Western blot and immunohistochemistry of the neurofilaments NF70 and NF200, as well as the protein levels of pre- and postsynaptic proteins SNAP25 and PSD95, failed to show obvious differences between *SARM1*$^{-/-}$, *SARM1*$^{+/-}$, and *SARM1*$^{+/+}$ mouse brains at 112 dpi (Fig. 2, M–V; and Fig. S1). This is in accordance with a previous report that slow Wallerian degeneration mice displayed unaltered prion pathogenesis (Gültner et al., 2009).

SARM1 deficiency does not alter prion-induced neuroinflammation

Upon challenge with WNV, *SARM1*$^{-/-}$ mice show increased viral replication in the brain stem and enhanced mortality associated with decreased microglial activation and reduced level of TNFα; Szretter et al., 2009). Therefore, we set out to assess the extent of neuroinflammation in prion-infected *SARM1*$^{-/-}$, *SARM1*$^{+/-}$, and *SARM1*$^{+/+}$ mice. We performed Iba1 immunohistochemical staining to evaluate microglial activation in *SARM1*$^{-/-}$, *SARM1*$^{+/-}$, and *SARM1*$^{+/+}$ mouse brains collected at 112 dpi and observed a

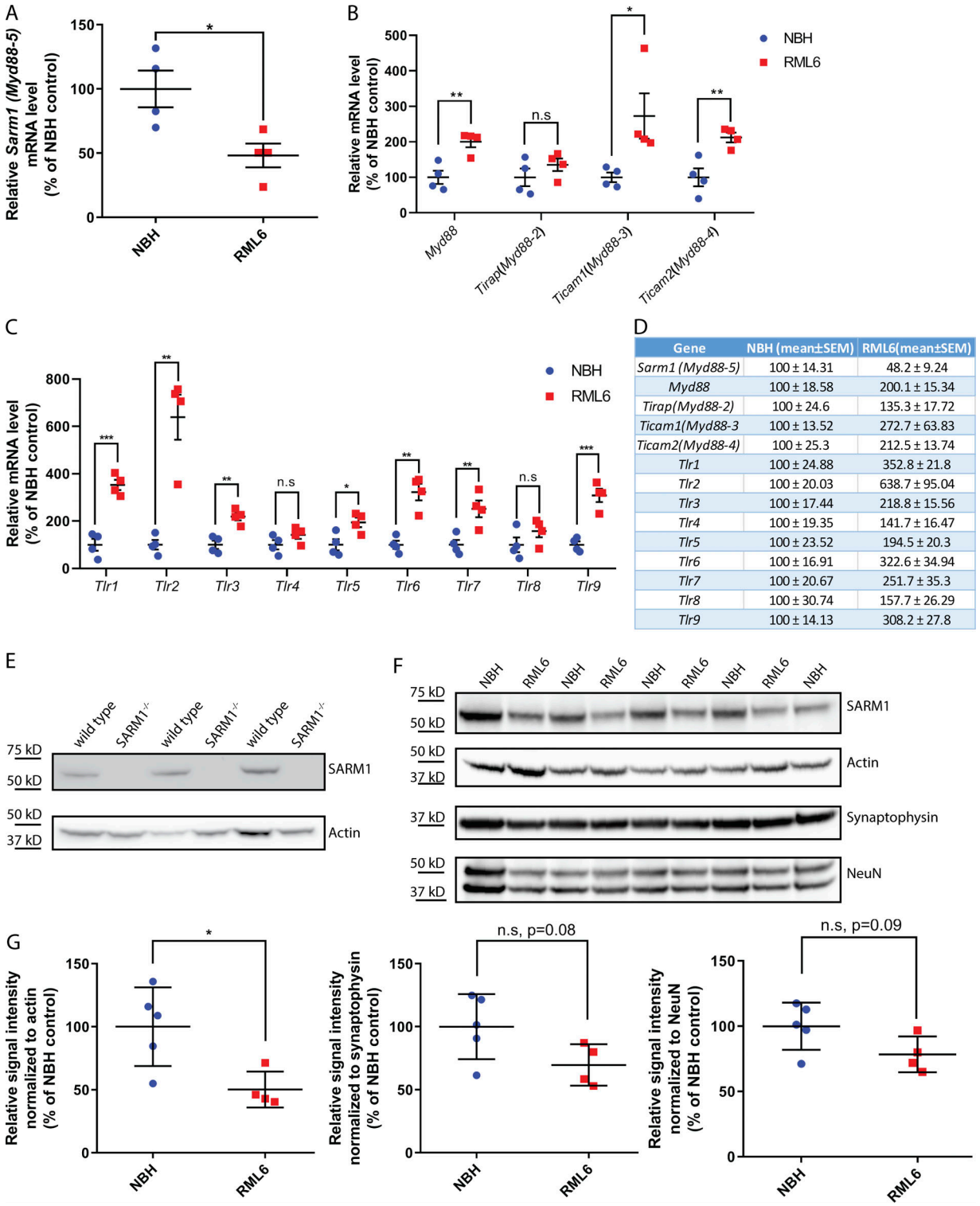

Gene	NBH (mean±SEM)	RML6(mean±SEM)
Sarm1 (Myd88-5)	100 ± 14.31	48.2 ± 9.24
Myd88	100 ± 18.58	200.1 ± 15.34
Tirap(Myd88-2)	100 ± 24.6	135.3 ± 17.72
Ticam1(Myd88-3	100 ± 13.52	272.7 ± 63.83
Ticam2(Myd88-4)	100 ± 25.3	212.5 ± 13.74
Tlr1	100 ± 24.88	352.8 ± 21.8
Tlr2	100 ± 20.03	638.7 ± 95.04
Tlr3	100 ± 17.44	218.8 ± 15.56
Tlr4	100 ± 19.35	141.7 ± 16.47
Tlr5	100 ± 23.52	194.5 ± 20.3
Tlr6	100 ± 16.91	322.6 ± 34.94
Tlr7	100 ± 20.67	251.7 ± 35.3
Tlr8	100 ± 30.74	157.7 ± 26.29
Tlr9	100 ± 14.13	308.2 ± 27.8

Figure 1. **Reduced expression of SARM1 in prion-infected mouse brains**. **(A–C)** qRT-PCR for *Sarm1* (A), MyD88 family (B), and TLR (C) mRNA from terminally sick RML6-infected C57BL/6 mice and age-matched NBH-inoculated C57BL/6 mice (n = 4). Relative expression was normalized to GAPDH expression and represented as the percentage of average values in NBH-treated mice. **(D)** Summary of the qRT-PCR results. **(E and F)** Western blot for SARM1, actin, Syp, and NeuN on brains collected from terminally sick RML6-infected C57BL/6 mice and NBH-inoculated C57BL/6 mice. **(G)** Densitometric quantification of the SARM1 Western blot. n = 5 for NBH-treated mice and n = 4 for RML6-treated mice. Relative signal intensity was represented as the percentage of average values in NBH-treated mice (n = 5). qRT-PCR and Western blot results represent at least three independent experiments. n.s., $P > 0.05$; *, $P < 0.05$; **, $P < 0.01$; ***, $P < 0.001$. Data are shown as mean ± SEM.

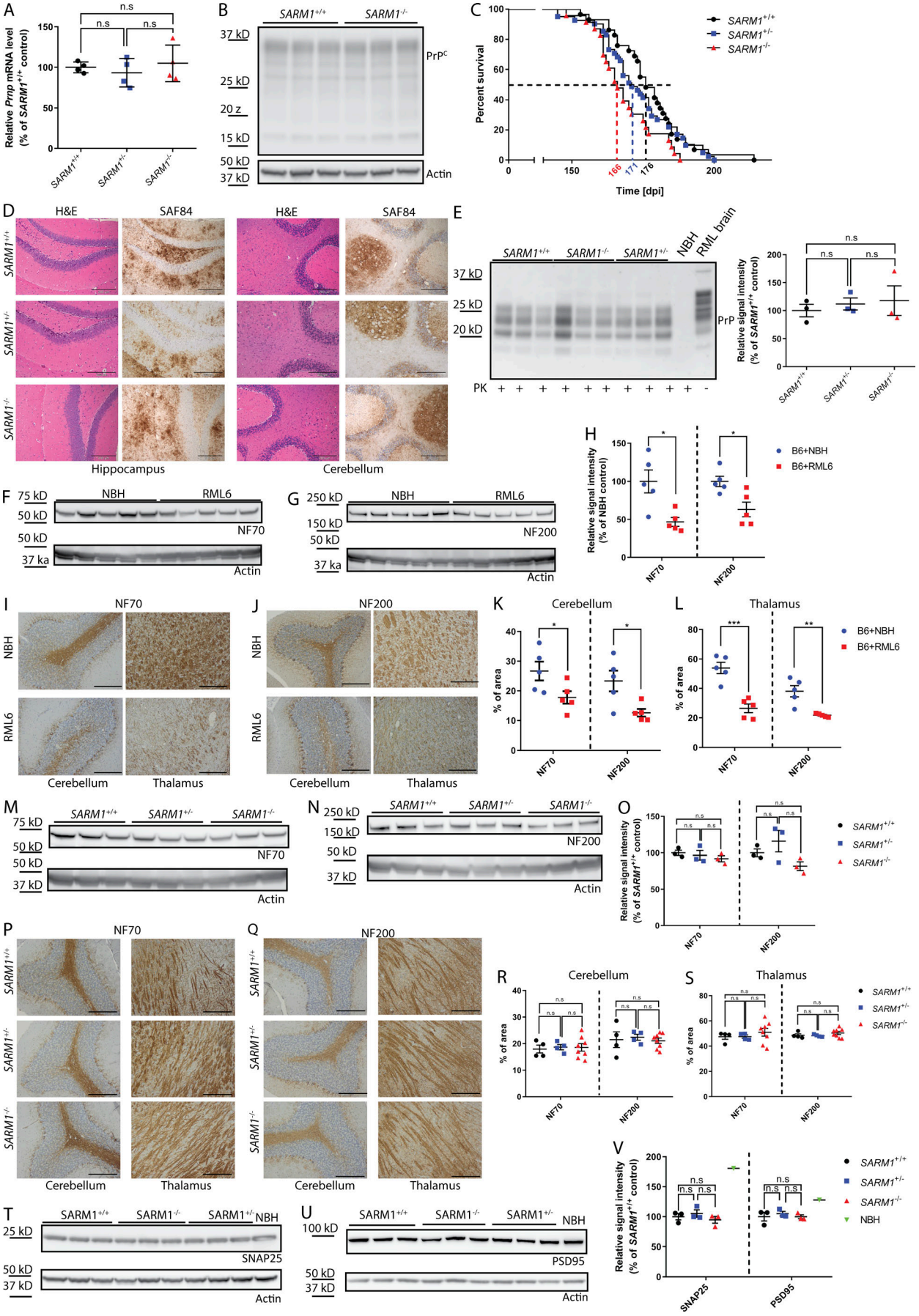

Figure 2. **SARM1 deficiency accelerated prion progression. (A)** qRT-PCR for *Prnp* mRNA in *SARM1*$^{-/-}$, *SARM1*$^{+/-}$, and *SARM1*$^{+/+}$ mouse brains. *n* = 4 for each genotype. **(B)** Western blot for PrP^{C} in *SARM1*$^{-/-}$ and *SARM1*$^{+/+}$ mouse brains. **(C)** Survival curves of RML6-infected *SARM1*$^{-/-}$, *SARM1*$^{+/-}$, and *SARM1*$^{+/+}$ mice. The median survival of *SARM1*$^{-/-}$ mice was 166 dpi (*n* = 23), whereas that of *SARM1*$^{+/+}$ mice was 176 dpi (*n* = 29). The median survival of *SARM1*$^{+/-}$ mice was 171 dpi (*n* = 41). The survival curves summarize three independent intracerebral inoculation experiments of 22, 25, and 46 mice, respectively. **(D)** H&E and immunostainings for SAF84 (which detects PrP) on RML6-infected *SARM1*$^{-/-}$, *SARM1*$^{+/-}$, and *SARM1*$^{+/+}$ brains at 112 dpi. Left: Hippocampus. Right: Cerebellum. Bars, 200 µm. **(E)** Left: PrP^{Sc} Western blot of RML6-infected *SARM1*$^{-/-}$, *SARM1*$^{+/-}$, and *SARM1*$^{+/+}$ brain homogenates at 112 dpi. Right: Densitometric quantification of the PrP^{Sc} Western blot. *n* = 3 for each genotype. **(F–L)** Western blot and immunohistochemistry of brain for NF70 (F and I) and NF200 (G and J) in terminally sick RML6-infected C57BL/6 mice and NBH-inoculated C57BL/6 mouse brains. **(H)** Densitometric quantification of NF70 and NF200 Western blot showing dramatic NF70 and NF200 reduction in RML6-infected brains. **(K and L)** Quantification of NF70 and NF200 staining in cerebellum (K) and thalamus (L) showed decreased NF70 and NF200 staining in RML6-infected brains. *n* = 5 for NBH-treated and RML6-treated mice. Bars, 200 µm. **(M–S)** Western blot and immunohistochemistry of brain tissues for NF70 (M and P) and NF200 (N and Q) in RML6-infected *SARM1*$^{-/-}$, *SARM1*$^{+/-}$, and *SARM1*$^{+/+}$ mouse brains at 112 dpi. **(O)** Densitometric quantification of NF70 and NF200 Western blots showed unchanged NF70 and NF200 levels. *n* = 3 for each genotype. **(R and S)** Quantification of NF70 and NF200 staining in cerebellum (R) and thalamus (S) showed unaltered NF70 and NF200 staining. *n* = 4 for *SARM1*$^{+/-}$ and *SARM1*$^{+/+}$ mice; *n* = 8 for *SARM1*$^{-/-}$ mice. Bars, 200 µm. **(T and U)** Western blots for SNAP25 (T) and PSD95 (U) in RML6-infected *SARM1*$^{-/-}$, *SARM1*$^{+/-}$, and *SARM1*$^{+/+}$ mouse brains at 112 dpi. **(V)** Densitometric quantification of the SNAP25 and PSD95 Western blots showed unchanged protein levels. *n* = 3 for each genotype. qRT-PCR, Western blot, and histology results represent at least three independent experiments. Relative signal intensity of Western blot was represented as the percentage of average values in NBH-treated or *SARM1*$^{+/+}$ mice. The immunohistochemical staining was calculated as the percentage of brown signals over the total area. n.s., P > 0.05; *, P < 0.05; **, P < 0.01; ***, P < 0.001. Data are shown as mean ± SEM.

similar level of microglial activation in all three groups (Fig. 3, A and B). Sholl analysis of the microglial morphology (Kongsui et al., 2014; Papageorgiou et al., 2016) showed a similar pattern of microglial activation between the three groups (Fig. 3 C). Western blot of Iba1 confirmed that *SARM1*$^{-/-}$, *SARM1*$^{+/-}$, and *SARM1*$^{+/+}$ mouse brains experienced similar levels of microglial activation (Fig. 3 D and Fig. S1). Additionally, we found a similar number of $CD68^{+}$ cells (representing activated microglia) in various regions in *SARM1*$^{-/-}$, *SARM1*$^{+/-}$, and *SARM1*$^{+/+}$ mouse brains (Fig. 3 E). Therefore, SARM1 deficiency does not alter prion-induced microglial activation. We also performed GFAP (glial fibrillary acidic protein) immunohistochemical staining to assess astrogliosis. There were no overt differences between the different genotypes (Fig. 3 F). Western blot of GFAP confirmed that *SARM1*$^{-/-}$, *SARM1*$^{+/-}$, and *SARM1*$^{+/+}$ mouse brains experienced similar levels of astrogliosis at 112 dpi (Fig. 3 G and Fig. S1). Furthermore, cytokine profiling showed similar levels of Tnfα, Il-1β, and Il-6 mRNAs in *SARM1*$^{-/-}$, *SARM1*$^{+/-}$, and *SARM1*$^{+/+}$ mouse brains at 112 dpi (Fig. 3 H). Therefore, SARM1 deficiency does not overtly alter prion-induced neuroinflammation.

The acceleration of prion pathogenesis by SARM1 ablation is consistent with findings in a WNV infection model, where *SARM1*$^{-/-}$ mice experienced enhanced mortality. However, the pathomechanisms appear to differ between WNV and prion infections. WNV-infected *SARM1*$^{-/-}$ mice showed decreased microglial activation and reduced levels of TNFα, whereas prion-infected *SARM1*$^{-/-}$ mice failed to show any difference in microglial activation, astrogliosis, or cytokine production.

SARM1 deficiency leads to XAF1 up-regulation and enhanced apoptosis

In an effort to discover how SARM1 deficiency accelerates prion progression, we performed whole-transcriptome analyses of *SARM1*$^{-/-}$ and *SARM1*$^{+/+}$ mouse brains with or without prion infection by RNA sequencing (RNaseq). Surprisingly, only very few genes were differentially expressed in *SARM1*$^{-/-}$ and *SARM1*$^{+/+}$ mouse brains. Of these, only SARM1 itself and XAF1 showed strong down- or up-regulation (fold change >2, P < 0.01) in both uninfected and prion-infected brains (Fig. 4, A and B; and Table S1). We then verified the RNaseq results by qRT-PCR. XAF1 mRNA was significantly up-regulated by SARM1 deficiency in a gene dose–dependent manner (Fig. 4 C). Interestingly, we observed that prion infection itself up-regulated XAF1 expression, even in the absence of SARM1 (Fig. 4 C). Therefore, prion infection and SARM1 deficiency synergistically up-regulated XAF1 expression in prion-infected *SARM1*$^{-/-}$ mice.

A previous study showed up-regulation of XAF1 mRNA in a different SARM1-deficient mouse line but claimed that XAF1 protein levels remained unaltered (Hou et al., 2013). We have tested several anti-XAF1 antibodies to detect increased levels of XAF1 protein in *SARM1*$^{-/-}$ and prion-infected mouse brains. However, all tested anti-XAF1 antibodies failed to detect a specific XAF1 band. The anti-XAF1 antibody from Aviva Systems Biology (OAAB14914) could detect transiently overexpressed XAF1 in mouse neuronal CAD5 cells (XAF1 mRNA >180-fold up-regulated) but not endogenous XAF1 in CAD5 cells or mouse brains (Fig. S2). Our results suggest that the failure of detecting increased levels of XAF1 protein is mainly due to the lack of specific and sufficiently sensitive anti-mouse XAF1 antibodies.

The murine XAF1 and SARM1 loci are both located on chromosome 11 with a distance of 2.75 cM. The ablation of the SARM1 gene may conceivably alter XAF1 expression by affecting the chromosomal structure of neighboring loci, or by cosegregating with polymorphic DNA loci. To test these possibilities, we performed siRNA silencing of SARM1 in CAD5 cells. Also in this paradigm, the knockdown of SARM1 significantly up-regulated XAF1 expression (Fig. 4, D–F; and Fig. S1). These results suggest that SARM1 regulates XAF1 expression in trans, and this regulation is cell autonomous. The mechanisms underlying this regulation may involve miRNAs and/or epigenetic regulation (Byun et al., 2003; Zou et al., 2006; Lee et al., 2011).

To further investigate whether SARM1 deficiency leads to up-regulation of XAF1 in a cell-autonomous manner in prion-infected mouse brains, we performed in situ hybridization of SARM1 and XAF1 on formalin-fixed, paraffin-embedded brain sections using the RNAscope technology. Again, we found that SARM1 and XAF1 mRNA signals colocalized predominantly in synaptophysin (Syp)-positive neurons and SARM1 deficiency

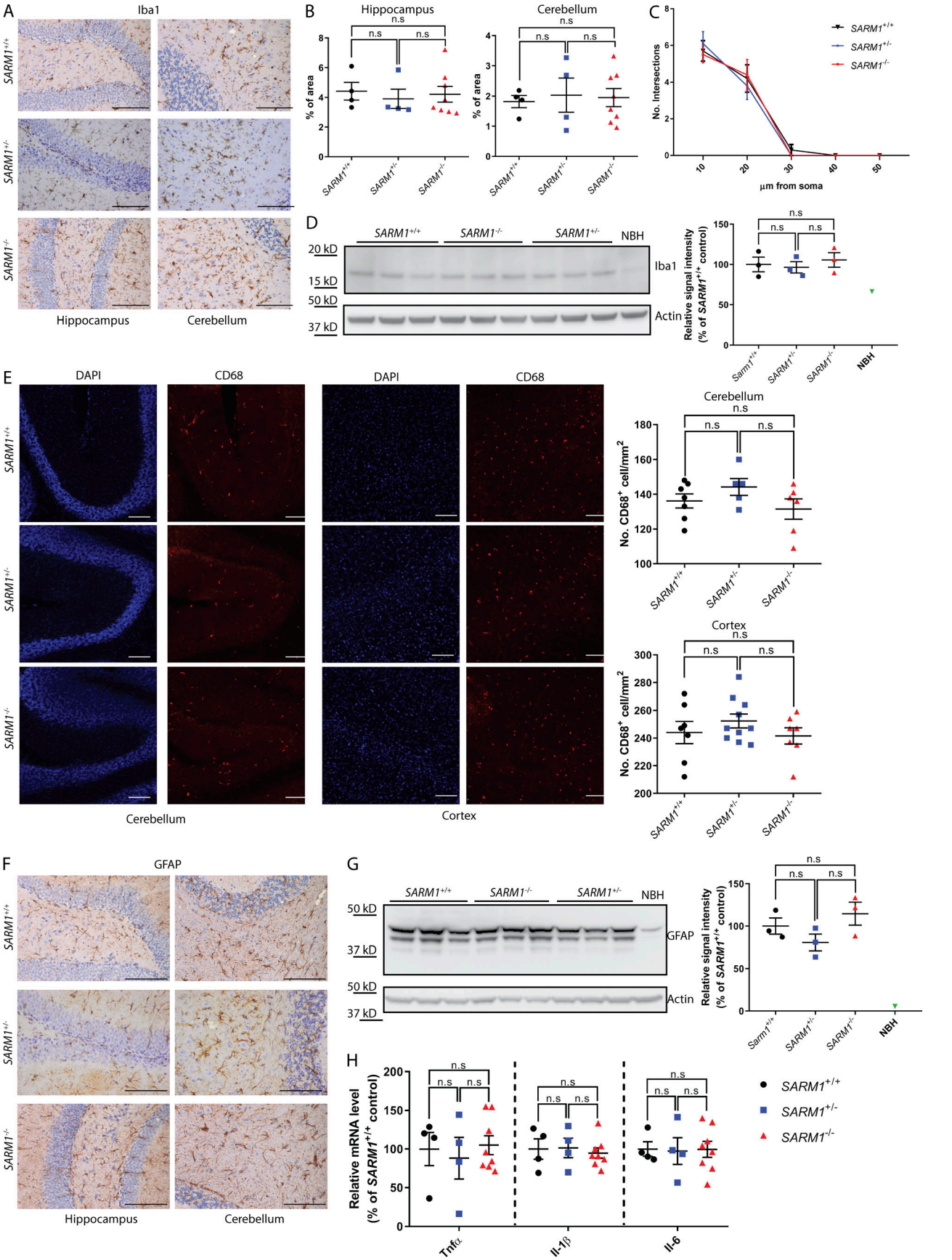

Figure 3. **Unaltered neuroinflammation in prion-infected SARM1$^{-/-}$ mouse brains. (A)** Iba1 immunohistochemistry of brain tissues from RML6-infected *SARM1*$^{-/-}$, *SARM1*$^{+/-}$, and *SARM1*$^{+/+}$ mice at 112 dpi. Bars, 100 µm. **(B)** Quantification of Iba1 staining in hippocampus (left) and cerebellum (right). *n* = 4 for *SARM1*$^{+/-}$ and *SARM1*$^{+/+}$ mice; *n* = 8 for *SARM1*$^{-/-}$ mice. **(C)** Sholl analysis of Iba1-positive microglia in RML6-infected *SARM1*$^{-/-}$, *SARM1*$^{+/-}$, and *SARM1*$^{+/+}$ mouse brains at 112 dpi. **(D)** Left: Western blot for Iba1 in RML6-infected *SARM1*$^{-/-}$, *SARM1*$^{+/-}$, and *SARM1*$^{+/+}$ mouse brains at 112 dpi. Right: Densitometric quantification of the Iba1 Western blot. *n* = 3 for each genotype. **(E)** Left: CD68 immunohistochemistry of brain tissues from RML6-infected *SARM1*$^{-/-}$, *SARM1*$^{+/-}$, and *SARM1*$^{+/+}$ mice at 112 dpi. Bars, 100 µm. Right: Quantification of CD68-positive cells. *n* = 5~10. **(F)** GFAP immunohistochemistry of brain tissues from RML6-infected *SARM1*$^{-/-}$, *SARM1*$^{+/-}$, and *SARM1*$^{+/+}$ mice at 112 dpi. Bars, 100 µm. **(G)** Left: Western blot for GFAP in RML6-infected *SARM1*$^{-/-}$, *SARM1*$^{+/-}$, and *SARM1*$^{+/+}$ mouse brains at 112 dpi. Right: Densitometric quantification of the GFAP Western blot. *n* = 3 for each genotype. **(H)** qRT-PCR of cytokines (Tnfα, Il-1β, and Il-6) in RML6-infected *SARM1*$^{-/-}$, *SARM1*$^{+/-}$, and *SARM1*$^{+/+}$ mouse brains at 112 dpi. *n* = 8 for *SARM1*$^{-/-}$ and *n* = 4 for *SARM1*$^{+/-}$ and *SARM1*$^{+/+}$ mice. Relative expression was normalized to GAPDH expression and represented as the percentage of average values in *SARM1*$^{+/+}$ mice. Histology, Western blot, and qRT-PCR results represent at least three independent experiments. Relative signal intensity of Western blot was represented as the percentage of average values in *SARM1*$^{+/+}$ mice. The immunohistochemical staining was calculated as the percentage of brown signals over the total area. n.s., P > 0.05. Data are shown as mean ± SEM.

increased XAF1 signals in neurons (Fig. 4 G). Interestingly, we also observed SARM1 signals in *SARM1*$^{-/-}$ mouse brains in which exons 1–2 are deleted, indicating that the RNAscope SARM1 probes (20 pairs of Z RNA probe targeting exons 2–6) could still recognize the truncated SARM1 transcripts containing exons 3–6. These results confirm that the up-regulation of XAF1 expression by SARM1 depletion in vivo is also cell autonomous.

XAF1 is a pro-apoptotic molecule that antagonizes the caspase-inhibitory activity of XIAP by redistributing XIAP from the cytosol to the nucleus (Liston et al., 2001). Abolishing XAF1 expression increases the resistance of cell lines to apoptosis, whereas overexpression of XAF1 sensitizes motoneurons to axotomy and the first trimester trophoblast cells to Fas-mediated apoptosis (Perrelet et al., 2004; Straszewski-Chavez et al., 2007). We therefore set out to assess whether SARM1-deficient mice might experience enhanced apoptosis after prion infection. We performed caspase 3 and caspase 9 activity assays by measuring their DEVDase and LEHDase activities, respectively. Indeed, RML6-infected *SARM1*$^{-/-}$ brains showed significantly higher caspase 3 and caspase 9 activity (Fig. 5, A and B) than SARM1$^{+/+}$ brains collected at 112 dpi. TUNEL (terminal deoxynucleotidyl transferase dUTP nick end labeling) staining showed that apoptosis was more prevalent in RML6-infected *SARM1*$^{-/-}$ brains than in *SARM1*$^{+/+}$ brains at 112 dpi (Fig. 5 C). Accordingly, the neuronal marker synapsin I, which was decreased in terminally prion-sick mice (Fig. 5 D and Fig. S1) but not altered by SARM1 deficiency in uninfected mice (Fig. 5 E), was significantly lower in prion-infected *SARM1*$^{-/-}$ brains at 112 dpi (Fig. 5 F and Fig. S1). These results suggest that SARM1 deficiency sensitizes mice to prion-induced apoptosis, leading to enhanced neuronal death.

It has been reported that XAF1 may cooperate with TNFα to induce apoptosis and increase expression of XAF1-sensitized cells to apoptosis (Xia et al., 2006; Straszewski-Chavez et al., 2007). To establish whether the enhanced susceptibility to apoptosis by SARM1 deficiency is due to the up-regulation of XAF1, we first silenced SARM1 in CAD5 cells and then treated them with TNFα. We found that while TNFα led to apoptosis and reduced cell numbers in both SARM1-silenced and nontarget siRNA treated cells, apoptosis was enhanced and cell numbers were more conspicuously reduced in SARM1-silenced cells (Fig. 5, G–I). However, when the same treatment was performed on XAF1 KO CAD5 cells generated by the CRISPR/Cas9 system (Fig. 5 J), the enhancement by SARM1 silencing was abrogated (Fig. 5, G–I), indicating that SARM1 deficiency sensitized cells to apoptotic stimuli mainly through the up-regulated XAF1. Therefore, it is conceivable that the deterioration of prion pathogenesis in *SARM1*$^{-/-}$ mice may be due to the up-regulated XAF1 and consequently enhanced apoptosis.

In summary, we found that SARM1 deficiency unexpectedly accelerated prion progression. SARM1 deficiency selectively up-regulated expression of the pro-apoptotic protein XAF1, which, in turn, enhanced apoptosis in prion-infected *SARM1*$^{-/-}$ mice. Since the effects appear to be gene-dosage dependent, XAF1 repression may potentially ameliorate prion-related neuronal pathologies.

Materials and methods

Ethical statement

All animal experiments were performed in strict accordance with the Rules and Regulations for the Protection of Animal Rights (Tierschutzgesetz and Tierschutzverordnung) of the Swiss Bundesamt für Lebensmittelsicherheit und Veterinärwesen and were preemptively approved by the Animal Welfare Committee of the Canton of Zürich (permit 41/2012).

Animals

SARM1$^{-/-}$ mice (Szretter et al., 2009) carrying a targeted deletion of exons 1–2 were first backcrossed to C57BL/6J to obtain *SARM*$^{+/-}$ offspring. *SARM*$^{+/-}$ mice were then intercrossed to obtain *SARM1*$^{-/-}$, *SARM*$^{+/-}$, and *SARM1*$^{+/+}$ (WT) littermates, which were used for the experiments described here. Mice were maintained in a high hygienic-grade facility and housed in groups of 3–5, under a 12-h light/12-h dark cycle (from 7 a.m. to 7 p.m.) at 21 ± 1°C, with sterilized food (3436; Provimi Kliba) and water provided ad libitum.

Intracerebral prion inoculation

Mice at 6–8 wk old were intracerebrally inoculated with 30 µl of brain homogenate diluted in PBS with 5% BSA and containing 3×10^5 LD_{50} units of the RML6. Scrapie was diagnosed according to clinical criteria (ataxia, kyphosis, priapism, and hind-leg paresis). Mice were sacrificed on the day of onset of terminal clinical signs of scrapie.

qRT-PCR

Total RNA from brain was extracted using TRIzol (Invitrogen Life Technologies) according to the manufacturer's instructions.

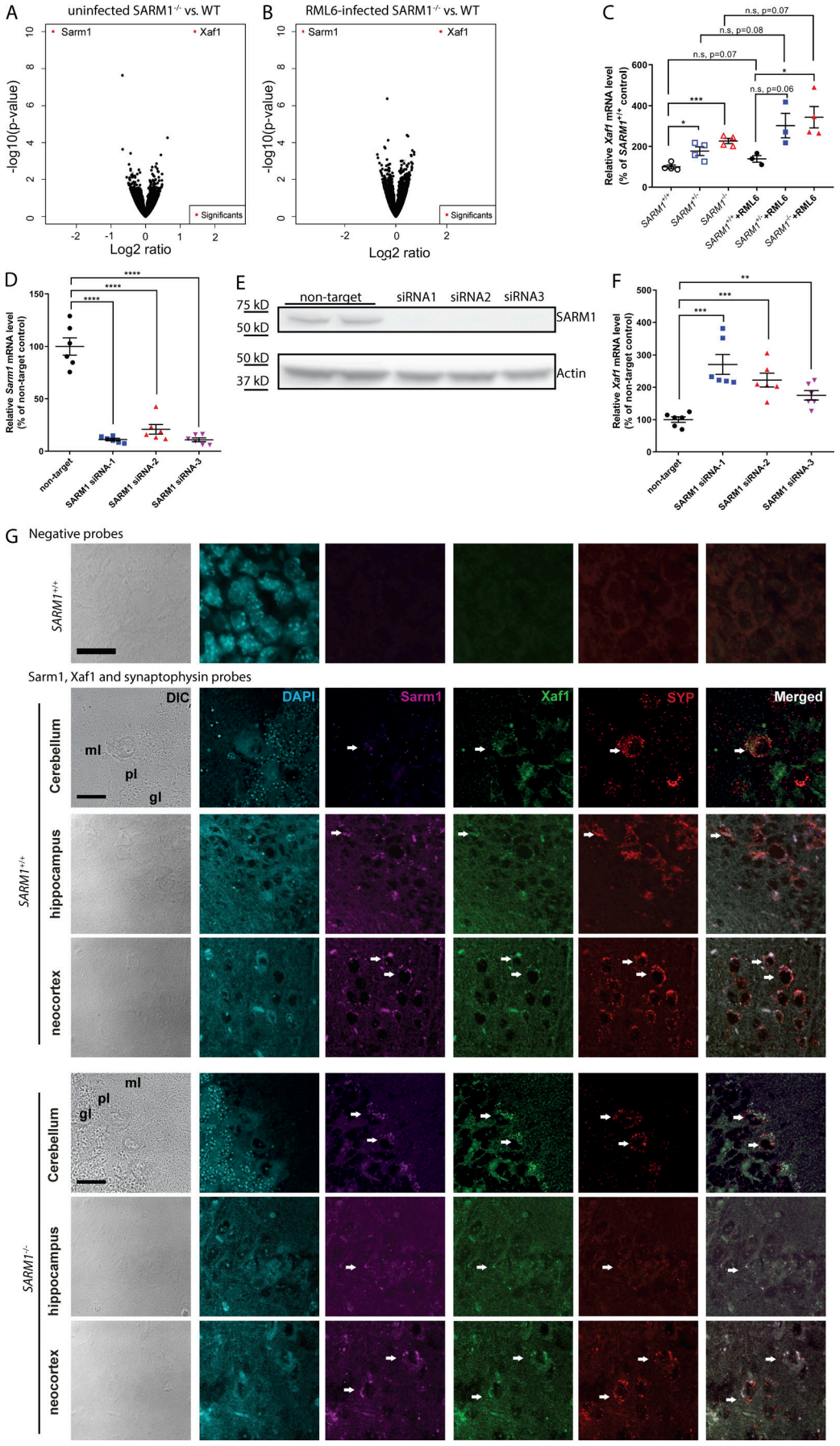

Figure 4. **SARM1 deficiency and prion infection up-regulated XAF1 expression in mouse brains. (A and B)** Volcano plots of RNaseq data for uninfected (A) and RML6-infected (112 dpi; B) *SARM1*$^{-/-}$ and WT mouse brains. Significants (red dots) are genes that show log2 ratios >1 or < −1 (fold change >2) with P < 0.01. **(C)** qRT-PCR of Xaf1 in uninfected and RML6-infected (112 dpi) *SARM1*$^{-/-}$, *SARM1*$^{+/-}$, and *SARM1*$^{+/+}$ mouse brains. *n* = 3–4 for each group. Relative expression was normalized to GAPDH expression and represented as the percentage of average values in uninfected *SARM1*$^{+/+}$ mice. **(D and E)** qRT-PCR of Sarm1 (D) and SARM1 Western blot (E) in SARM1 siRNA-treated CAD5 cells. **(F)** qRT-PCR of Xaf1 in SARM1 siRNA-treated CAD5 cells. *n* = 6 for each treatment. Relative expression was normalized to GAPDH expression and represented as the percentage of average values in nontarget control. **(G)** Upper panel: Images of in situ hybridization using 3-Plex negative probes. Middle and lower panels: Representative images of Sarm1, Xaf1, and Syp in situ hybridization in RML6-infected WT (middle) and *SARM1*$^{-/-}$ (lower) mouse cerebella, hippocampi, and neocortex at 112 dpi. Differential interference contrast (DIC) and DAPI staining show the morphology and nuclei of cells. gl, granular layer; ml, molecular layer; pl, Purkinje cell layer. White arrows indicate Sarm1, Xaf1, and Syp triple-positive cells. Bars, 20 µm. qRT-PCR and Western blot results represent at least three independent experiments. In situ hybridization represents two independent experiments. n.s., P > 0.05; *, P < 0.05; **, P < 0.01; ***, P < 0.001; ****, P < 0.0001. Data are shown as mean ± SEM.

The quality of RNA was analyzed by Bioanalyzer 2100 (Agilent Technologies); RNAs with an RNA integrity number >7 were used for cDNA synthesis. cDNAs were synthesized from ∼1 µg total RNA using a QuantiTect Reverse Transcription kit (Qiagen) according to the manufacturer's instructions. qRT-PCR was performed using the SYBR Green PCR Master Mix (Roche) on a ViiA7 Real-Time PCR system (Applied Biosystems).

The following primer pairs were used: GAPDH sense 5′-CCA CCCCAGCAAGGAGACT-3′; antisense, 5′-GAAATTGTGAGGGAG ATGCT-3′; Sarm1 (Myd88-5) sense, 5′-CGCTGCCCTGTACTG GAGG-3′; antisense, 5′-CTTCAGGAGGCTGGCCAGCT-3′; Myd88 sense, 5′-TCATGTTCTCCATACCCTTGGT-3′; antisense, 5′-AAA CTGCGAGTGGGGTCAG-3′; Tirap (Myd88-2) sense, 5′-CCTCCT CCACTCCGTCCAA-3′; antisense, 5′-CTTTCCTGGGAGATCGGC AT-3′; Ticam1 (Myd88-3) sense, 5′-CCAGCTCAAGACCCCTAC AG-3′; antisense, 5′-CAAGGCACCTAGAATGCCAAA-3′; Ticam2 (Myd88-4) sense, 5′-CGATCAAGACGGCCATGAGTC-3′; anti-sense, 5′-CTCGTCGGTGTCATCTTCTGC-3′; Tlr1 sense, 5′-TGA GGGTCCTGATAATGTCCTAC-3′; antisense, 5′-AGAGGTCCAAAT GCTTGAGGC-3′; Tlr2 sense, 5′-GCAAACGCTGTTCTGCTCAG-3′; antisense, 5′-AGGCGTCTCCCTCTATTGTATT-3′; Tlr3 sense, 5′-GTGAGATACAACGTAGCTGACTG-3′; antisense, 5′-TCCTGCATC CAAGATAGCAAGT-3′; Tlr4 sense, 5′-AGGCACATGCTCTAGCAC TAA-3′; antisense, 5′-AGGCTCCCCAGTTTAACTCTG-3′; Tlr5 sense, 5′-GCAGGATCATGGCATGTCAAC-3′; antisense, 5′-ATC TGGGTGAGGTTACAGCCT-3′; Tlr6 sense, 5′-TGAGCCAAGACA GAAAACCCA-3′; antisense, 5′-GGGACATGAGTAAGGTTCCTG TT-3′; Tlr7 sense, 5′-ATGTGGACACGGAAGAGACAA-3′; anti-sense, 5′-GGTAAGGGTAAGATTGGTGGTG-3′; Tlr8 sense, 5′-GAAAACATGCCCCCTCAGTCA-3′; antisense, 5′-CGTCACAAG GATAGCTTCTGGAA-3′; Tlr9 sense, 5′-ATGGTTCTCCGTCGA AGGACT-3′; antisense, 5′-GAGGCTTCAGCTCACAGGG-3′; Tnfα sense, 5′-CATCTTCTCAAAATTCGAGTGACAA-3′; antisense, 5′-TGGGAGTAGACAAGGTACAACCC-3′; Il-1β sense, 5′-CAACCA ACAAGTGATATTCTCCATG-3′; antisense, 5′-GATCCACACTCT CCAGCTGCA-3′; Il-6 sense, 5′-TCCAATGCTCTCCTAACAGAT AAG-3′; antisense, 5′-CAAGATGAATTGGATGGTCTTG-3′; and Xaf1 sense, 5′-GAAGCTTGACCATGGAGGCT-3′; antisense, 5′-GGTGCACAACTTCCATGTGCT-3′. Expression levels were normalized using GAPDH.

Western blot analysis

To detect SARM1 and PrP^{C} in the mouse brains, one hemisphere from each brain was homogenized with buffer PBS containing 0.5% Nonidet P-40 and 0.5% 3-([3-cholamidopropyl] dimethylammonio)-2-hydroxy-1-propanesulfonate (CHAPSO). Total protein concentration was determined using the bicinchoninic acid assay (Pierce). Approximately 20 µg protein were loaded and separated on a 12% Bis-Tris polyacrylamide gel (NuPAGE; Invitrogen) and then blotted onto a nitrocellulose membrane. Membranes were blocked with 5% wt/vol Topblock (LuBioScience) in PBS supplemented with 0.05% Tween 20 (vol/vol) and incubated with primary antibodies anti-SARM1 (D2M5I) rabbit mAb (1:1,000; 13022; Cell Signaling Technology) or POM1 (200 ng/ml) in 1% Topblock overnight. After washing, the membranes were then incubated with secondary antibody HRP-conjugated goat anti-rabbit IgG (1:10,000; 111-035-045; Jackson ImmunoResearch) or goat anti–mouse IgG (1:10,000; 115-035-003; Jackson ImmunoResearch). Blots were developed using Luminata Crescendo Western HRP substrate (Millipore) and visualized using the Stella system (model 3200; Raytest). To avoid variation in loading, the same blots were stripped and incubated with an anti-actin antibody (1:10,000; MAB1501R; Millipore). The signals were normalized to actin as a loading control. To detect PrP^{Sc} in prion-infected *SARM1*$^{-/-}$, *SARM*$^{+/-}$, and *SARM1*$^{+/+}$ (WT) mouse brains, prion-infected forebrains were homogenized in sterile 0.32 M sucrose in PBS. Total protein concentration was determined using the bicinchoninic acid assay (Pierce). Samples were adjusted to 20 µg protein in a 20 µl prepared solution and digested with 25 µg/ml PK in digestion buffer (PBS containing 0.5% wt/vol sodium deoxycholate and 0.5% vol/vol Nonidet P-40) for 30 min at 37°C. PK digestion was stopped by adding loading buffer (Invitrogen) and boiling samples at 95°C for 5 min. Proteins were then separated on a 12% Bis-Tris polyacrylamide gel (NuPAGE; Invitrogen) and blotted onto a nitrocellulose membrane. POM1 and HRP-conjugated goat anti-mouse IgG were used as primary and secondary antibodies, respectively. Blots were developed using Luminata Crescendo Western HRP substrate (Millipore) and visualized using the Fujifilm LAS-3000 system. To detect NeuN, Syp, NF70, NF200, SNAP25, PSD95, Iba-1, GFAP, and synapsin I in prion-infected WT C57BL/6 mouse brains or *SARM1*$^{-/-}$, *SARM1*$^{+/-}$, and *SARM1*$^{+/+}$ (WT) mouse brains, 20 µg of total brain protein were loaded and anti-NeuN clone EPR12763 (ab177487; Abcam), anti-synaptophysin clone 2/Syp (611880; BD Biosciences), anti–neurofilament-L clone DA2 (1:1,000; 2835; Cell Signaling Technology), anti-neurofilament 200 clone NE14 (1:1,000; N5389; Sigma), anti-SNAP25 antibody (1:1,000; ab5666; Abcam), anti-PSD95 antibody (1:1,000; 18258; Abcam), anti–Iba-1 antibody (1:1,000; Wako

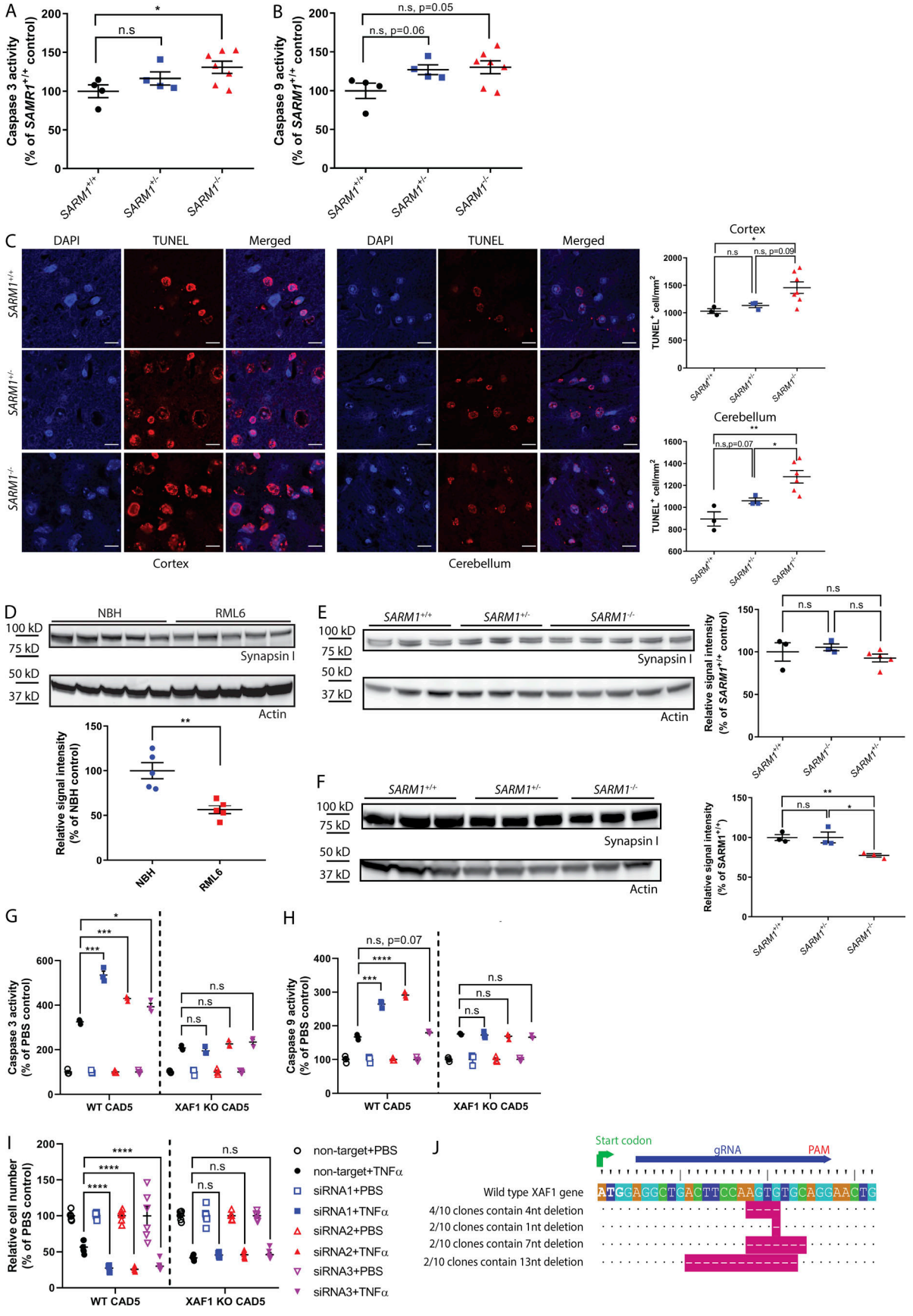

Figure 5. **SARM1 deficiency enhanced apoptosis in prion-infected SARM1$^{-/-}$ brains. (A and B)** Caspase 3 (A) and caspase 9 (B) activity assay of RML6-infected *SARM1*$^{-/-}$, *SARM1*$^{+/-}$, and *SARM1*$^{+/+}$ mouse brains at 112 dpi. *n* = 8 for *SARM1*$^{-/-}$ and *n* = 4 for *SARM1*$^{+/-}$ and *SARM1*$^{+/+}$ mice. Relative caspase 3 and caspase 9 activity was represented as the percentage of average values in *SARM1*$^{+/+}$ mice. **(C)** Left: TUNEL staining of brain tissues from RML6-infected *SARM1*$^{-/-}$, *SARM1*$^{+/-}$, and *SARM1*$^{+/+}$ mice at 112 dpi. Right: Quantification of TUNEL-positive cells. *n* = 7 for *SARM1*$^{-/-}$ and *n* = 3 for *SARM1*$^{+/-}$ and *SARM1*$^{+/+}$ mice. Bars, 10 µm. **(D)** Upper: Western blot for synapsin I on brains collected from terminally sick RML6-infected C57BL/6 mice and NBH-inoculated C57BL/6 mice. Lower: Densitometric quantification of the synapsin I Western blot showed a significant reduction of synapsin I in RML6-infected brains. *n* = 5 for NBH-treated and RML6-treated mice. **(E)** Left: Western blot for synapsin I in uninfected *SARM1*$^{-/-}$, *SARM1*$^{+/-}$, and *SARM1*$^{+/+}$ mice. Right: Densitometric quantification of the synapsin I Western blots showed unchanged synapsin I level in uninfected *SARM1*$^{-/-}$, *SARM1*$^{+/-}$, and *SARM1*$^{+/+}$ mice. *n* = 3 for *SARM1*$^{+/-}$ and *SARM1*$^{+/+}$ mice; *n* = 5 for *SARM1*$^{-/-}$ mice. **(F)** Left: Western blot for synapsin I in RML6-infected *SARM1*$^{-/-}$, *SARM1*$^{+/-}$, and *SARM1*$^{+/+}$ mouse brains at 112 dpi. Right: Densitometric quantification of the synapsin I Western blot. *n* = 3 for each genotype. **(G)** Caspase 3 activity assay of WT CAD5 and XAF1 KO CAD5 cell lysates after SARM1 siRNAs and TNFα treatments. **(H)** Caspase 9 activity assay of WT CAD5 and XAF1 KO CAD5 cell lysates after SARM1 siRNAs and TNFα treatments. *n* = 3. Relative caspase 3 and caspase 9 activity was represented as the percentage of average values in PBS groups. **(I)** RealTime-Glo assay of live WT CAD5 and XAF1 KO CAD5 cells after SARM1 siRNAs and TNFα treatments. *n* = 6. Relative cell numbers were represented as the percentage of average values in PBS groups. Relative caspase 3 and caspase 9 activity measurement represents two independent experiments. **(J)** Sequencing results of the Xaf1 gene in XAF1 KO CAD5 cells showed that the coding sequence of all sequenced clones was frameshifted. PAM, protospacer adjacent motif. Western blot results represent at least three independent experiments. Relative signal intensity of Western blot was represented as the percentage of average values in NBH-treated or *SARM1*$^{+/+}$ mice. n.s., P > 0.05; *, P < 0.05; **, P < 0.01; ***, P < 0.001; ****, P < 0.0001. Data are shown as mean ± SEM.

Chemicals GmbH), anti-GFAP antibody (D1F4Q) XP Rabbit mAb (1:3,000; 12389; Cell Signaling Technology), and anti-synapsin I (1:2,000; AB1543; Millipore AG) were used. To detect XAF1 in mouse brains and CAD5 cells, primary antibodies rabbit anti-mouse XAF1 antibody (1:1,000; ab17204 and ab81353 [Abcam]; OAAB14914 [Aviva Systems Biology]; A03432 [Boster]; PA1-41099 [Invitrogen]; GTX51339 [GeneTex]; NB100-56355 [Novus Biologicals]) were used. Actin was used as a loading control.

Immunohistochemistry

For immunohistochemistry of prion-infected brains, formalin-fixed tissues were treated with concentrated formic acid for 60 min to inactivate prion infectivity and embedded in paraffin. Paraffin sections (2 µm) of brains were stained with H&E. After deparaffinization through graded alcohols, Iba-1 antibody (1:1,000; Wako Chemicals GmbH) was used for highlighting microglial cells, GFAP antibody (1:300; DAKO) was used for astrocytes, anti-neurofilament 70 clone 2F11 (1:100; M076229-2; DAKO) and anti-neurofilament 200 clone NE14 (1:2,000; N5389; Sigma) antibodies were used for assessing axonal degeneration. Stainings were visualized using an IVIEW DAB Detection Kit (Ventana), with a hematoxylin counterstain applied subsequently. For the histological detection of partially PK-resistant prion protein deposition, deparaffinized sections were pretreated with formaldehyde for 30 min and with 98% formic acid for 6 min, and then washed in distilled water for 30 min. Sections were incubated in Ventana buffer, and stains were performed on a NEXEX immunohistochemistry robot (Ventana) using an IVIEW DAB Detection Kit (Ventana). After incubation with protease 1 (Ventana) for 16 min, sections were incubated with anti-PrP SAF-84 (1:200; A03208; SPI Bio) for 32 min. Sections were counterstained with hematoxylin. Sections were imaged using a Zeiss Axiophot light microscope. Quantification of Iba-1, GFAP, NF70, and NF200 staining was performed on acquired images, where regions of interest were drawn, and the percentage of brown Iba-1, GFAP, NF70, and NF200 staining over the total area was quantified using ImageJ software (National Institutes of Health). For CD68 staining, 4% paraformaldehyde-fixed brain tissues were cut into 10-µm cryosections and stained with anti-CD68 antibody clone FA-11 (MCA1957; Bio-Rad) and visualized by Alexa 546 conjugated goat-anti-rat antibody (A11081; Invitrogen). The nuclei were counterstained with DAPI. Images were captured using confocal laser scanning microscope FluoView Fv10i (Olympus). The operator was blinded to the genotype and treatment of the analyzed tissues.

RNaseq

Total RNA from brain was extracted using TRIzol (Invitrogen Life Technologies) according to the manufacturer's instruction, followed by RNA cleanup using an RNeasy kit (Qiagen). The quality of RNA was analyzed by Bioanalyzer 2100 (Agilent Technologies), RNAs with RNA integrity number >8 were further processed. The TruSeq Stranded mRNA Sample Prep Kit (Illumina, Inc.) was used in the succeeding steps. Briefly, total RNA samples (500 ng) were poly-A selected and then reverse-transcribed into double-stranded cDNA with actinomycin added during first-strand synthesis. The cDNA samples were fragmented, end-repaired, and adenylated before ligation of TruSeq adapters. The adapters contain the index for multiplexing. Fragments containing TruSeq adapters on both ends were selectively enriched with PCR. The quality and quantity of the enriched libraries were validated using Qubit (1.0) Fluorometer (Life Technologies) and the Bioanalyzer 2100 (Agilent Technologies). The product is a smear with an average fragment size of ~360 bp. The libraries were normalized to 10 nM in Tris-Cl 10 mM, pH 8.5, with 0.1% Tween 20. The TruSeq SR Cluster Kit v4-cBot-HS (Illumina, Inc.) was used for cluster generation using 8 pM of pooled normalized libraries on the cBOT. Sequencing was performed on the Illumina HiSeq 4000 single-end 125 bp using the TruSeq SBS Kit v4-HS (Illumina, Inc.). Reads were quality-checked with FastQC. For RNaseq data analysis, we used RSEM to perform RNaseq read alignment and expression estimation (Li and Dewey, 2011). As reference we used the GRCm38 genome assembly and the corresponding gene annotations provided by Ensembl. We computed differential expression with the Bioconductor package DESeq2 (Love et al., 2014). A gene was considered as differentially expressed by applying a threshold of

0.01 for the P value and 1 for the log-ratio. Additionally, we filtered away genes that had very low counts. Specifically, we did not consider a gene as expressed if it did not exceed in at least one condition an average read count of 10 in the samples. All clusterings and visualizations were performed with R/Bioconductor (R version 3.2). Data from RNaseq analyses have been deposited to the Gene Expression Omnibus under the dataset code GSE124932.

Establishment of XAF1 KO CAD5 cells by CRISPR/Cas9

A XAF1 knockout CAD5 cell line was established by CRISPR/Cas9 genome editing approach. Briefly, a guide RNA targeting exon 1 of the XAF1 gene (5′-AGGCTGACTTCCAAGTGTGC-3′) was cloned into the pKLV-U6gRNA(BbsI)-PGKpuro2ABFP vector (Addgene 50946) to generate pKLV-XAF1 single guide RNA plasmid. CAD5 cells were cotransfected with pKLV-XAF1 single guide RNA and pCMV-hCas9 (Addgene 41815) in a molar ratio of 1:1 by Lipofectamine 2000 (11668-019; Invitrogen). Transfected cells were selected and enriched by puromycin (2 µg/ml), and single-cell clones were obtained by limited dilution. Cell clones were grown and expanded. To confirm gene editing of the XAF1 gene in cell clones, a region embracing exon 1 of the XAF1 gene was PCR-amplified using a forward primer (5′-GTCACAGTCACG GTAGCACA-3′) and reverse primer (5′-GGGACCAGTCCCTCC ATACT-3′); the PCR product was cloned into pCR-Blunt II-TOPO vector (45-0245; Invitrogen) and sequenced to verify the frameshifted indels.

siRNA and TNFα treatment on CAD5 and XAF1 KO CAD5 cells

24 h before transfection, 2×10^5 CAD5 cells (murine neuronal cell line) per well were seeded in 6-well plates. CAD5 cells were then transfected with three different SARM1 siRNA (siRNA ID: s108645, s108646, and s108647; Thermo Fisher Scientific) or nontarget negative control siRNA (4390843; Thermo Fisher Scientific) at 50 nM concentration using Lipofectamine RNAiMAX. 48 h after transfection, cells were harvested for total RNA extraction and protein analysis.

For TNFα treatment, 2×10^4 CAD5 or XAF1 KO CAD5 cells per well were first seeded in 96-well plates and transfected with SARM1 siRNAs or nontarget negative control siRNA. 24 h after the transfection, cells were treated with TNFα at a concentration of 50 ng/ml or PBS control for 72 h. Cell viability was assessed by RealTime-Glo (G9713; Promage). The relative cell viability was calculated as percentages to the PBS control groups.

RNAscope in situ hybridization

Transcripts of SARM1, XAF1, and Syp in formalin-fixed, paraffin-embedded brain sections were detected by in situ hybridization using RNAscope Multiplex Fluorescent Reagent Kit v2 (323100; Advanced Cell Diagnostics) following the manufacturer's instructions. Briefly, sections were deparaffinized and pretreated with hydrogen peroxide and protease plus, followed by hybridization with target probes (SARM1, 504191-C2; XAF1, 504181; Syp, 426521-C3), which are designed and manufactured by Advanced Cell Diagnostics. 3-Plex negative control probes targeting the DapB gene from the *Bacillus subtilis* strain SMY (320871) were used as a negative control. After amplification steps, fluorescence signals were developed by TSA Plus fluorophores kits (fluorescein, NEL741E001KT; Cyanine 3, NEL744E001KT; Cyanine 5, NEL745001KT; PerkinElmer). Images were captured using a Leica TCS SP5 confocal microscope.

Caspase 3 and caspase 9 activity assay

Caspase 3 activity was measured by a caspase 3 assay kit (ab39401; Abcam) and caspase 9 activity was measured by a caspase 9 assay kit (ab65608; Abcam) according to the manufacturer's instructions. Briefly, brain homogenates or cell lysates containing the same amount of total protein were incubated with either DEVE-p-NA or LEHD-p-NA substrates. After cleavage, the p-NA light emission was quantified using a microtiter plate reader at 405 nm. The activity of caspase 3 and caspase 9 was calculated as percentages to the $SARM1^{+/+}$ (WT) control or cell lysates treated with PBS.

TUNEL assay

Apoptosis in paraffin sections of prion-infected mouse brains were assessed by an in situ BrdU-Red DNA fragmentation assay kit according to the manufacturer's instructions (ab66110; Abcam). Briefly, sections were deparaffinized and treated with PK, followed by labeling of DNA nicks with Br-dUTP (bromolated deoxyuridine triphosphate nucleotide) mediated by terminal deoxynucleotidyl transferase. The incorporated BrdU was detected by fluorescently labeled anti-BrdU monoclonal antibody. The nuclei were counterstained with DAPI. Images were captured using confocal laser scanning microscope FluoView Fv10i (Olympus) and analyzed using ImageJ software (National Institutes of Health).

Statistical analysis

Results are presented as the mean of replicas ± SEM. Unpaired Student's *t* test was used for comparing two samples. For in vivo experiments, all groups were compared by log-rank (Mantel-Cox) test. P values <0.05 were considered statistically significant.

Online supplemental material

Fig. S1 shows full images of the cropped Western blots in main figures, Fig. S2 shows the validation of various XAF1 antibodies by Western blot. Table S1 presents the RNaseq results.

Acknowledgments

We thank the team of the Institute of Neuropathology, University Hospital Zurich, and in particular, I. Abakumova, R. Moos, J. Guo, M. Delic, K. Arroyo, and M. König for technical assistance. We thank Elisabeth J. Rushing for reading the manuscript and offering suggestions and Marco Colonna for providing us with *SARM1*$^{-/-}$ mice.

A. Aguzzi is the recipient of an Advanced Grant of the European Research Council (grant 250356) and is supported by grants from the GELU Foundation, the Swiss National Foundation (including a Sinergia grant), SystemsX.ch, the Swiss Personalized Health Network, the Nomis Foundation, and the Klinische Forschungsschwerpunkte "small RNAs" and "Human Hemato-Lymphatic Diseases." K. Frontzek is a recipient of a

grant from the Theodor und Ida Herzog-Egli Stiftung. The funders had no role in study design, data collection and analysis, decision to publish, or preparation of the manuscript.

The authors declare no competing financial interests.

Author contributions: C. Zhu and A. Aguzzi conceived and designed the overall study. C. Zhu and B. Li performed most experiments and interpreted the data. K. Frontzek contributed to the generation of the XAF1 KO CAD5 cell line and captured in situ hybridization images. Y. Liu performed the RNAscope in situ hybridization. C. Zhu, B. Li, and A. Aguzzi wrote the manuscript.

Submitted: 16 October 2017
Revised: 27 November 2018
Accepted: 11 January 2019

References

Aguzzi, A., and C. Zhu. 2012. Five questions on prion diseases. *PLoS Pathog.* 8: e1002651. https://doi.org/10.1371/journal.ppat.1002651

Aguzzi, A., and C. Zhu. 2017. Microglia in prion diseases. *J. Clin. Invest.* 127: 3230–3239. https://doi.org/10.1172/JCI90605

Aguzzi, A., M. Nuvolone, and C. Zhu. 2013. The immunobiology of prion diseases. *Nat. Rev. Immunol.* 13:888–902. https://doi.org/10.1038/nri3553

Byun, D.S., K. Cho, B.K. Ryu, M.G. Lee, M.J. Kang, H.R. Kim, and S.G. Chi. 2003. Hypermethylation of XIAP-associated factor 1, a putative tumor suppressor gene from the 17p13.2 locus, in human gastric adenocarcinomas. *Cancer Res.* 63:7068–7075.

Carty, M., R. Goodbody, M. Schröder, J. Stack, P.N. Moynagh, and A.G. Bowie. 2006. The human adaptor SARM negatively regulates adaptor protein TRIF-dependent Toll-like receptor signaling. *Nat. Immunol.* 7:1074–1081. https://doi.org/10.1038/ni1382

Conforti, L., J. Gilley, and M.P. Coleman. 2014. Wallerian degeneration: an emerging axon death pathway linking injury and disease. *Nat. Rev. Neurosci.* 15:394–409. https://doi.org/10.1038/nrn3680

Essuman, K., D.W. Summers, Y. Sasaki, X. Mao, A. DiAntonio, and J. Milbrandt. 2017. The SARM1 Toll/interleukin-1 receptor domain possesses intrinsic NAD+ cleavage activity that promotes pathological axonal degeneration. *Neuron.* 93:1334–1343.e5.

Ferrer, I. 2002. Synaptic pathology and cell death in the cerebellum in Creutzfeldt-Jakob disease. *Cerebellum.* 1:213–222. https://doi.org/10.1080/14734220260418448

Geisler, S., R.A. Doan, A. Strickland, X. Huang, J. Milbrandt, and A. DiAntonio. 2016. Prevention of vincristine-induced peripheral neuropathy by genetic deletion of SARM1 in mice. *Brain.* 139:3092–3108. https://doi.org/10.1093/brain/aww251

Gerdts, J., D.W. Summers, Y. Sasaki, A. DiAntonio, and J. Milbrandt. 2013. Sarm1-mediated axon degeneration requires both SAM and TIR interactions. *J. Neurosci.* 33:13569–13580. https://doi.org/10.1523/JNEUROSCI.1197-13.2013

Gerdts, J., E.J. Brace, Y. Sasaki, A. DiAntonio, and J. Milbrandt. 2015. SARM1 activation triggers axon degeneration locally via NAD$^+$ destruction. *Science.* 348:453–457. https://doi.org/10.1126/science.1258366

Gerdts, J., D.W. Summers, J. Milbrandt, and A. DiAntonio. 2016. Axon self-destruction: new links among SARM1, MAPKs, and NAD+ metabolism. *Neuron.* 89:449–460. https://doi.org/10.1016/j.neuron.2015.12.023

Goniotaki, D., A.K.K. Lakkaraju, A.N. Shrivastava, P. Bakirci, S. Sorce, A. Senatore, R. Marpakwar, S. Hornemann, F. Gasparini, A. Triller, and A. Aguzzi. 2017. Inhibition of group-I metabotropic glutamate receptors protects against prion toxicity. *PLoS Pathog.* 13:e1006733. https://doi.org/10.1371/journal.ppat.1006733

Gray, B.C., Z. Siskova, V.H. Perry, and V. O'Connor. 2009. Selective presynaptic degeneration in the synaptopathy associated with ME7-induced hippocampal pathology. *Neurobiol. Dis.* 35:63–74. https://doi.org/10.1016/j.nbd.2009.04.001

Grizenkova, J., S. Akhtar, S. Brandner, J. Collinge, and S.E. Lloyd. 2014. Microglial Cx3cr1 knockout reduces prion disease incubation time in mice. *BMC Neurosci.* 15:44. https://doi.org/10.1186/1471-2202-15-44

Guiroy, D.C., S.K. Shankar, C.J. Gibbs Jr., J.A. Messenheimer, S. Das, and D.C. Gajdusek. 1989. Neuronal degeneration and neurofilament accumulation in the trigeminal ganglia in Creutzfeldt-Jakob disease. *Ann. Neurol.* 25: 102–106. https://doi.org/10.1002/ana.410250119

Gültner, S., M. Laue, C. Riemer, I. Heise, and M. Baier. 2009. Prion disease development in slow Wallerian degeneration (Wld(S)) mice. *Neurosci. Lett.* 456:93–98. https://doi.org/10.1016/j.neulet.2009.03.089

Henninger, N., J. Bouley, E.M. Sikoglu, J. An, C.M. Moore, J.A. King, R. Bowser, M.R. Freeman, and R.H. Brown Jr. 2016. Attenuated traumatic axonal injury and improved functional outcome after traumatic brain injury in mice lacking Sarm1. *Brain.* 139:1094–1105. https://doi.org/10.1093/brain/aww001

Herrmann, U.S., A.K. Schütz, H. Shirani, D. Huang, D. Saban, M. Nuvolone, B. Li, B. Ballmer, A.K. Åslund, J.J. Mason, et al. 2015. Structure-based drug design identifies polythiophenes as antiprion compounds. *Sci. Transl. Med.* 7:299ra123. https://doi.org/10.1126/scitranslmed.aab1923

Hou, Y.J., R. Banerjee, B. Thomas, C. Nathan, A. García-Sastre, A. Ding, and M.B. Uccellini. 2013. SARM is required for neuronal injury and cytokine production in response to central nervous system viral infection. *J. Immunol.* 191:875–883. https://doi.org/10.4049/jimmunol.1300374

Jeffrey, M., J.R. Fraser, W.G. Halliday, N. Fowler, C.M. Goodsir, and D.A. Brown. 1995. Early unsuspected neuron and axon terminal loss in scrapie-infected mice revealed by morphometry and immunocytochemistry. *Neuropathol. Appl. Neurobiol.* 21:41–49. https://doi.org/10.1111/j.1365-2990.1995.tb01027.x

Kim, Y., P. Zhou, L. Qian, J.Z. Chuang, J. Lee, C. Li, C. Iadecola, C. Nathan, and A. Ding. 2007. MyD88-5 links mitochondria, microtubules, and JNK3 in neurons and regulates neuronal survival. *J. Exp. Med.* 204:2063–2074. https://doi.org/10.1084/jem.20070868

Kongsui, R., S.B. Beynon, S.J. Johnson, and F.R. Walker. 2014. Quantitative assessment of microglial morphology and density reveals remarkable consistency in the distribution and morphology of cells within the healthy prefrontal cortex of the rat. *J. Neuroinflammation.* 11:182. https://doi.org/10.1186/s12974-014-0182-7

Lee, J.E., E.J. Hong, H.Y. Nam, J.W. Kim, B.G. Han, and J.P. Jeon. 2011. MicroRNA signatures associated with immortalization of EBV-transformed lymphoblastoid cell lines and their clinical traits. *Cell Prolif.* 44:59–66. https://doi.org/10.1111/j.1365-2184.2010.00717.x

Li, B., and C.N. Dewey. 2011. RSEM: accurate transcript quantification from RNA-Seq data with or without a reference genome. *BMC Bioinformatics.* 12:323. https://doi.org/10.1186/1471-2105-12-323

Liberski, P.P., and H. Budka. 1999. Neuroaxonal pathology in Creutzfeldt-Jakob disease. *Acta Neuropathol.* 97:329–334. https://doi.org/10.1007/s004010050995

Liberski, P.P., H. Budka, R. Yanagihara, and D.C. Gajdusek. 1995. Neuroaxonal dystrophy in experimental Creutzfeldt-Jakob disease: electron microscopical and immunohistochemical demonstration of neurofilament accumulations within affected neurites. *J. Comp. Pathol.* 112:243–255. https://doi.org/10.1016/S0021-9975(05)80078-7

Liston, P., W.G. Fong, N.L. Kelly, S. Toji, T. Miyazaki, D. Conte, K. Tamai, C.G. Craig, M.W. McBurney, and R.G. Korneluk. 2001. Identification of XAF1 as an antagonist of XIAP anti-Caspase activity. *Nat. Cell Biol.* 3:128–133. https://doi.org/10.1038/35055027

Loreto, A., M. Di Stefano, M. Gering, and L. Conforti. 2015. Wallerian degeneration is executed by an NMN-SARM1-dependent late Ca(2+) influx but only modestly influenced by mitochondria. *Cell Reports.* 13: 2539–2552. https://doi.org/10.1016/j.celrep.2015.11.032

Love, M.I., W. Huber, and S. Anders. 2014. Moderated estimation of fold change and dispersion for RNA-seq data with DESeq2. *Genome Biol.* 15: 550. https://doi.org/10.1186/s13059-014-0550-8

Mukherjee, P., T.A. Woods, R.A. Moore, and K.E. Peterson. 2013. Activation of the innate signaling molecule MAVS by bunyavirus infection upregulates the adaptor protein SARM1, leading to neuronal death. *Immunity.* 38:705–716. https://doi.org/10.1016/j.immuni.2013.02.013

Osterloh, J.M., J. Yang, T.M. Rooney, A.N. Fox, R. Adalbert, E.H. Powell, A.E. Sheehan, M.A. Avery, R. Hackett, M.A. Logan, et al. 2012. dSarm/Sarm1 is required for activation of an injury-induced axon death pathway. *Science.* 337:481–484. https://doi.org/10.1126/science.1223899

Papageorgiou, I.E., A. Lewen, L.V. Galow, T. Cesetti, J. Scheffel, T. Regen, U.K. Hanisch, and O. Kann. 2016. TLR4-activated microglia require IFN-γ to induce severe neuronal dysfunction and death in situ. *Proc. Natl. Acad. Sci. USA.* 113:212–217. https://doi.org/10.1073/pnas.1513853113

Perrelet, D., F.E. Perrin, P. Liston, R.G. Korneluk, A. MacKenzie, M. Ferrer-Alcon, and A.C. Kato. 2004. Motoneuron resistance to apoptotic cell death in vivo correlates with the ratio between X-linked inhibitor of apoptosis proteins (XIAPs) and its inhibitor, XIAP-associated factor 1. *J. Neurosci.* 24: 3777–3785. https://doi.org/10.1523/JNEUROSCI.0413-04.2004

Reis, R., E. Hennessy, C. Murray, E.W. Griffin, and C. Cunningham. 2015. At the centre of neuronal, synaptic and axonal pathology in murine prion disease: degeneration of neuroanatomically linked thalamic and brainstem nuclei. *Neuropathol. Appl. Neurobiol.* 41:780–797. https://doi.org/10.1111/nan.12232

Sakai, K., R. Hasebe, Y. Takahashi, C.H. Song, A. Suzuki, T. Yamasaki, and M. Horiuchi. 2013. Absence of CD14 delays progression of prion diseases accompanied by increased microglial activation. *J. Virol.* 87:13433–13445. https://doi.org/10.1128/JVI.02072-13

Sasaki, Y., T. Nakagawa, X. Mao, A. DiAntonio, and J. Milbrandt. 2016. NMNAT1 inhibits axon degeneration via blockade of SARM1-mediated NAD^+ depletion. *eLife.* 5:e19749. https://doi.org/10.7554/eLife.19749

Sorce, S., M. Nuvolone, A. Keller, J. Falsig, A. Varol, P. Schwarz, M. Bieri, H. Budka, and A. Aguzzi. 2014. The role of the NADPH oxidase NOX2 in prion pathogenesis. *PLoS Pathog.* 10:e1004531. https://doi.org/10.1371/journal.ppat.1004531

Straszewski-Chavez, S.L., I.P. Visintin, N. Karassina, G. Los, P. Liston, R. Halaban, A. Fadiel, and G. Mor. 2007. XAF1 mediates tumor necrosis factor-alpha-induced apoptosis and X-linked inhibitor of apoptosis cleavage by acting through the mitochondrial pathway. *J. Biol. Chem.* 282:13059–13072. https://doi.org/10.1074/jbc.M609038200

Szretter, K.J., M.A. Samuel, S. Gilfillan, A. Fuchs, M. Colonna, and M.S. Diamond. 2009. The immune adaptor molecule SARM modulates tumor necrosis factor alpha production and microglia activation in the brainstem and restricts West Nile Virus pathogenesis. *J. Virol.* 83: 9329–9338. https://doi.org/10.1128/JVI.00836-09

Walker, L.J., D.W. Summers, Y. Sasaki, E.J. Brace, J. Milbrandt, and A. DiAntonio. 2017. MAPK signaling promotes axonal degeneration by speeding the turnover of the axonal maintenance factor NMNAT2. *eLife.* 6:6. https://doi.org/10.7554/eLife.22540

Xia, Y., R. Novak, J. Lewis, C.S. Duckett, and A.C. Phillips. 2006. Xaf1 can cooperate with TNFalpha in the induction of apoptosis, independently of interaction with XIAP. *Mol. Cell. Biochem.* 286:67–76. https://doi.org/10.1007/s11010-005-9094-2

Yang, J., Z. Wu, N. Renier, D.J. Simon, K. Uryu, D.S. Park, P.A. Greer, C. Tournier, R.J. Davis, and M. Tessier-Lavigne. 2015. Pathological axonal death through a MAPK cascade that triggers a local energy deficit. *Cell.* 160:161–176. https://doi.org/10.1016/j.cell.2014.11.053

Zhu, C., U.S. Herrmann, J. Falsig, I. Abakumova, M. Nuvolone, P. Schwarz, K. Frauenknecht, E.J. Rushing, and A. Aguzzi. 2016. A neuroprotective role for microglia in prion diseases. *J. Exp. Med.* 213:1047–1059. https://doi.org/10.1084/jem.20151000

Zou, B., C.S. Chim, H. Zeng, S.Y. Leung, Y. Yang, S.P. Tu, M.C. Lin, J. Wang, H. He, S.H. Jiang, et al. 2006. Correlation between the single-site CpG methylation and expression silencing of the XAF1 gene in human gastric and colon cancers. *Gastroenterology.* 131:1835–1843. https://doi.org/10.1053/j.gastro.2006.09.050